Bima memo 73 - May 1999

IMAGE FIDELITY

M.C.H. Wright
Radio Astronomy laboratory, University of California, Berkeley, CA, 94720

ABSTRACT

This memo discusses the imaging properties of the combined BIMA & OVRO arrays. The 15-antenna array with 8 GHz bandwidth and a system temperature 100 K will have a sensitivity 1 mJy min$^{-0.5}$. For extended sources the image fidelity depends on the source brightness distribution and data sampling. For mosaic observations the heterogeneous array comprised of 10.4 and 6.1 m antennas will have three different primary beam types. We compare the image fidelity obtained as a function of the *uv* sampling, the pointing sampling, and the image complexity, and compare these results with imaging by a homogeneous array of 8 m antennas.

1. Introduction

Image quality is usually described by the thermal noise level and by the dynamic range (the ratio of the peak brightness to the off-source RMS). The *image fidelity* - how closely the image represents the real source distribution - depends not only on the thermal noise but also on other errors in the data, such as amplitude, phase, and pointing errors, and also on imaging artifacts.

Many astronomical studies require a comparison of the brightness distribution of different images. If these images can be obtained simultaneously with the same instrument (e.g. multiple molecular lines), then common amplitude and phase errors or common *uv* coverage may minimize the effects of image errors. Other measurements such as time dependent source variations (e.g. VLBI observations), or spectral index distributions (e.g. supernova remnants), require comparison of images with different *uv* coverage and primary beams.

For weak emission, the image noise is consistent with the thermal noise level. For emission in the field of a strong quasar, the dynamic range is a good measure of the image noise level. For complex sources the image noise is harder to determine. In a recent study of the supernova remnant Cas A, we made a mosaiced image at 83 GHz with the BIMA array. Data with 19 pointing centers were combined with single dish data to form a well sampled image. The BIMA image was compared with VLA images at 1.4 and 5 GHz to look for spectral index variations across Cas A. We found that the image fidelity was critically dependent on adequate *uv* sampling. By combining data from 75 to 87 GHz and using multiple configurations of the 10-antenna BIMA array we obtained an image fidelity 1% to 2% of the peak flux density (1.5× the thermal noise). Residual amplitude and phase errors, and primary beam and pointing errors each contribute about 1% to the image errors.

The merged BIMA & OVRO arrays will have two or more antenna sizes. In order to get the full sensitivity of the combined array, cross correlations between all antennas should be made. With 2 antenna types, there are 3 different primary beam patterns; with N antenna types there are N(N+1)/2 patterns. Images of sources smaller than the primary beam of the largest antenna are independent of the mixed primary beam patterns. For larger sources, where mosaic observations are required, the effect of the mixed primary beams is significant, as discussed in bima memo 59. A large number of questions require detailed study.

This memo presents an empirical study of the image fidelity obtained as a function of the *uv* sampling, the pointing sampling, and the image complexity, and compares these results with images obtained with a homogeneous array.

2. The Merged Array

It is proposed to merge the BIMA & OVRO arrays at a high altitude site to form a new array, currently known as CARMA (Combined Array for Research in Millimeter-wave Astronomy). The combined array will have six 10.4 m antennas and nine 6.1 m antennas. For the purpose of this memo we assume the following characteristics:

* 5-arm scaled array configurations with resolutions 1, 2.5, 6.3″, and a compact array with 18″ resolution at 100 Ghz. (Mundy, 1998)

* 8 Ghz continuum bandwidth

* System temperature, Tsys=100K, 2 sidebands and 1 polarization (or Tsys=60K, 1 sideband and 1 polarization)

* Gaussian Primary beam patterns.

2.1. Sensitivity

The collecting area of six 10.4 m + ten 6.1 m antennas, for which the array configurations were designed, is equivalent to sixteen 8.0 m antennas. One of the 6.1 m antennas, antenna 3, was a prototype for the nine newer 6.1 m antennas, and differs in a number of important details, such as cabin size, drive system, and surface accuracy. Antenna 3 would need extensive work to bring it's 1 mm performance to the level of the other antennas, and would continue to need special attention. If this antenna is not used in the merged array then the six 10.4 m + nine 6.1 m antennas are equivalent to fifteen 8.1 m antennas in collecting area. The difference in collecting area is only 4%. A strong case cannot be made here for using antenna 3 in the merged array.

With fifteen antennas and the above assumptions, the continuum source sensitivity is 1 mJy $\mathrm{min}^{-0.5}$; the spectral line brightness sensitivity is 16 K $\mathrm{min}^{-0.5}$ in a 1 km/s channel at 100 GHz with a $1''$ beam. This assumes that all cross correlations (105 baselines) are made. Almost half of the sensitivity is lost if cross correlations between the 10.4 m and 6.1 m antennas are not made. For comparison, the current ten antenna BIMA array has the same continuum sensitivity in 5 hours, and the same spectral line sensitivity in 35 minutes.

3. Mapping Extended Sources

For mosaic observations, a heterogeneous array can be considered as a set of sub-arrays for each primary beam pattern resulting from the cross correlations of 6.1 m x 6.1 m, 10.4 m x 10.4 m, and 6.1 m x 10.4 m antennas. The primary beam pattern for the 6.1 m x 10.4 m correlations has a negative response within the primary beam of the 6.1 m antennas. The beam pattern depends on the illumination of the antennas. In practice the mosaicing algorithms usually clip the primary beam response at the 5 % level, thus avoiding the uncertainties and variations in the primary beam response at low levels. Within the 5 % level, the primary beam pattern from the 6.1 m x 10.4 m correlations is well approximated by the Gaussian beam pattern for an equivalent $sqrt(10.4 \times 6.1) = 8.0$ m antenna, conveniently close to the average collecting area per antenna.

3.1. Sampling requirements

Sampling rates are set by both the largest and smallest antenna diameter. The Nyquist *uv* data sample interval, δuv = D/2λ. The number of pointings, Npts = $\Omega/(\lambda/2\mathrm{D})^2$. Thus the Nyquist sampling rate = baseline/λ x $(2\mathrm{D}_{max}/\lambda)^2$ x $2\lambda/\mathrm{D}_{min}$ x Ω x sdot (D=antenna diameter, Ω=source size, and sdot=$2\pi/24/3600$). The *uv* data for each pointing are oversampled by the larger antennas, and the pointing is oversampled by the smaller antennas. There is no loss in sensitivity since the oversampled data are properly accounted for in the imaging algorithms, but it does increase the bulk of *uv* data compared with an homogeneous array. It is best to sample all pointings within the same *uv* cell (common pointing, calibration, etc), but Npts is limited by the maximum available sampling rates and by the antenna slew and settle times. On-the-fly (OTF) mosaicing may help, but requires synchronous slew of the antennas and fringe rates.

3.2. Observing strategies

The smaller antennas are well suited for mapping large source structure, and are best placed at short baselines in order to sample *uv* spacings down to the diameter of the smallest antenna. Mosaicing algorithms can recover visibilities about half a dish diameter shorter than the shortest measured spacing (e.g. Cornwell, 1988). A direct Fourier transform of the uv data w.r.t pointing center to generate more closely sampled uv data (Ekers & Rots 1979; BIMA memo 45), also extends the sampled uv data by about 0.5 to 0.7 of a dish diameter.

Shorter uv spacings can be obtained, either from single dish observations, or from interferometer observations with even smaller antennas. Both options may be available if the combined array is augmented by Carlstrom's array of 2.5 m antennas. Without Carlstrom's array, then it is best to outfit one or more 10.4 m antenna for single dish observations to overlap the shortest spacings sampled with the 6.1 m antennas. If Carlstrom's antennas are routinely available to sample uv spacings down to 2.5 m, then single dish observations with the 6.1 m antennas would suffice to supply the missing short spacings. Another issue is the sensitivity of the single dish observations. For many projects it is desirable to have approximately the same single dish sensitivity as the interferometer data. This is important for detecting and mapping large angular size sources, especially transient sources such as comets. This argues for using several of the 10.4 m antennas for single dish observations.

Placing the larger antennas at the longest radii on the radial array configurations provides a more uniform sensitivity in the uv data. Using the larger antennas on the longest interferometer baselines also reduces the required uv data sample rate ($2\lambda/D$).

4. Point source Imaging

We imaged a model composed of eight point sources with flux density: 1, 0.5, 0.3, 0.2, 0.1, 0.05, 0.02, and 0.01 Jy. The model was added to randomly sampled points within a circular annulus between 5 and 100 kλ. Random noise was added to the sampled uv data which was imaged with a $0.5''$ cell size and 512×512 pixels. The images were deconvolved using the CLEAN algorithm, which is well matched to deconvolving a field of point sources.

A single point source can be imaged with very few uv points. As the source becomes more complex, sidelobes from different parts of the source interfere with each other and it may not be possible to deconvolve the source perfectly in the presence of noise. In figure 1 and 2 we show the result of imaging eight point sources with 1000, 2000, and 4000 uv samples. The image noise was a constant 1 mJy per beam, and the images were deconvolved using the Clark Clean algorithm with up to 10000 iterations to ensure that the images were not limited by deconvolution errors. With only 1000 uv samples there are many spurious sources at the 1% level and a 20% error in the measured flux density of the 50 mJy source. With 2000 uv samples there are several spurious sources at the 0.3% level. With 4000 uv samples there are no spurious sources at the 0.3% level, although several appear at the 0.2% level and there is 20% error in the measured flux density of the 10 mJy source. In all cases, the RMS noise is close to the theoretical noise level of 1 mJy/beam, and the dynamic range is 1000:1

The level at which spurious sources appear, or the maximum difference between the image and model are useful measures of the image fidelity, but these are hard to use if the real source distribution is unknown. Empirical estimates of the image fidelity may be obtained by varying the imaging parameters and measuring the RMS differences between the sources on the ensemble of acceptable images.

For sufficiently simple models it may be possible to improve the image fidelity by first subtracting well determined sources from the *uv* data. We have not done this here as we wish to estimate the image fidelity for cases where this is not possible.

5. Cas A Imaging

We made images of Cas A using a VLA image as a model. Cas A is a complex source; the VLA model contains structures on all scales from $0.4''$ to $5'$. The VLA image was sampled with spatial frequencies corresponding to 4 configurations of 16 antennas with the CARMA array. We used the CARMA **b, c, d** and **e** antenna configurations (Mundy 1998), and two frequency channels. The compact **e** array was simply a scaled version of the **b** array with a minimum *uv* spacing of 3 m, to represent the potential gain from using Carlstrom's 2.5 m antennas. This was not optimized in any way. The model *uv* data, with added noise appropriate for the combined array, was imaged and deconvolved using the Maximum Entropy Algorithm (MEM) .

5.1. *uv* sampling

This first study does not model mosaicing. It is only a study of the effect of *uv* sampling with the CARMA configurations. The *uv* data were sampled at 1 min intervals with a thermal noise corresponding to a system temperature 100 K with a 1 Ghz bandwidth for each frequency channel. Observations at 100 and 108 GHz produce complementary *uv* points, and could be obtained at the same time if we had 8 GHz system bandwidth - or as separate observations if we have a smaller bandwidth. We made images using multifrequency synthesis (MFS) and deconvolved using the MEM algorithm with 50 iterations.

We added model *uv* data, one configuration at a time. With the d-configuration and 1 frequency channel at 100 GHz, we get $5.8'' \times 4.8''$ resolution and recover 22% of the total flux density. With c+d configurations and 2 frequency channels, we get $2.9'' \times 2.5''$ resolution and recover 32% of the total flux density. With c+d+e configurations and 2 frequency channels, we get $2.9'' \times 2.5''$ resolution and recover 48% of the total flux density. With b+c+d+e configurations and 2 frequency channels we get $2.1'' \times 1.8''$ resolution, and recover 65% of the total flux density. This image (Figure 3) is almost indistinguishable by eye from the VLA image convolved to the same resolution. Residual images were formed by subtracting the VLA model image convolved to the same resolution. The residual image for Cas A looks like the surface of the moon; large scale missing flux with error hills and craters close to bright features where MEM has not done so well.

The RMS on the residual image is 3.4 mJy/beam which is 3.5% of the peak on the convolved VLA image. The off-source RMS is 0.5 mJy/beam, and the thermal noise with 16 antennas, a system temperature 100 K, and 2 frequency channels is 30 micro Jy. Clearly neither the thermal noise nor the dynamic range is a good estimate of the image fidelity.

From this study, we conclude that: i) The image fidelity improves with the density of sampled uv points. ii) The recovered flux density depends on the shortest uv spacings. iii) The residual image shows the missing large scale structure (corresponding to spacings less than 3 m - which needs single dish data), and shows deconvolution errors on the strongest peaks, where MEM does not do a good job.

If only 10 antennas are used, then equally good images can be made with about 10/16 times the resolution, or with 16/10 times as many configurations (although we did not try all combinations), so this is not a strong justification for more antennas, but it is an endorsement of the CARMA array configurations, the need for a more compact configuration, and a large bandwidth.

5.2. Mosaic observations

We imagined the Cas A model with 19 pointings in a hexagonal mosaic with $1'$ spacings and with a 36 s sample interval. Figure 4 shows a single pointing on Cas A weighted by the three primary beam patterns obtained with 6.1 m and 10.4 m antennas. We used frequency channels at 80 and 88 Ghz to maintain Nyquist sampling of the pointings. With the b+c+d+e configurations and 2 frequency channels we get $2.8'' \times 2.4''$ resolution and the mosaiced image recovered 91% of the total flux density. The residual image, after subtracting the VLA model convolved to the same resolution, has an RMS error 1.4% of the peak on the mosaiced image. Adding 2 more frequency channels (at 83 and 86 GHz) did not improve the image fidelity significantly. The mosaiced image has recovered most of the large scale structure, but there is an error pattern with an angular scale of $1' - 2'$ corresponding to the shortest spacings sampled.

We increased the mosaic pattern to 37 pointings with $50''$ spacings at 100 GHz. The RMS residual is then 0.4% and the total flux density recovered is 94%. Increasing the sample interval to 3 minutes increased the RMS residual to 4%. The antennas move 10.8 m in 3 min on the longest baseline used (827 m), so the uv data for each pointing are poorly sampled. A 36 s sample interval with 37 pointings is already undersampled on the longest baseline. Increasing the sample interval to 3 minutes degrades the image significantly.

The above tests all used a minimum uv-spacing of 3 m for the e-array. Using a minimum spacing 6 m with 37 pointings and a 36s sample interval recovered only 54% of the total flux. The mosaic observations with a minimum spacing of 6 m did not recover quite as much of the total flux density as the single field observations with a minimum spacing of 3 m.

6. Eye charts

For neither the eight point source model nor the Cas A model is it easy to assess the image fidelity. For the point source model, errors in the measured flux densities and spurious sources are the most significant defects. For the Cas A model we used both the RMS difference between the image and the model, and the recovered total flux density as measures of the image fidelity. In general, errors can occur on all angular scales and it is not clear what is the best measure of image fidelity. In this section we analyse images of an eye chart model. The eye chart contains structures on a range of angular scales from $0.5''$ to $90''$, and it is easy to visually assess the image defects. The eye chart model has 23264 out of 303408 sampled pixels. Imaged at a resolution of $2.13'' \times 1.65''$, the effective beam area is 15.86 pixels, so that there are 1467 pieces of information in a field of 19130 resolution elements.

6.1. Random *uv* sampling

Randomly sampled *uv* points create a standard against which array configurations can be measured if the uniformity or efficiency of *uv* coverage is the criteria of success. For simple sources, well sampled *uv* tracks, with large gaps between them may be better suited to measure model parameters. However, large gaps can hide any source structure whose visibility has not been measured, so for complex sources, any gap in the sampled *uv* plane can detract from the image fidelity.

Figure 5 shows the effect of *uv* sampling on the image fidelity with 5000, 10^4, 10^5, and 10^6 *uv* points. Clearly, 5000 *uv* points are inadequate for this image. The image quality steadily improved as the number of *uv* points was increased.

A completely sampled *uv* plane can be Fourier transformed to form an image which is perfect down to the resolution limit of the sampled *uv* data. We verified that a Fourier transform of the eye chart and inverse transform back again to the image plane, reproduced the original model to the limits of the single precision arithmetic (10^{-5}) used in the the Miriad software.

6.2. Various Array Configurations

Figure 6 shows the same eye chart sampled by various array configurations. These are single field images (with an effectively infinite primary beam) to compare the effect of *uv* sampling with the different arrays. The arrays were scaled to the same resolution using the 5-armed CARMA configurations for 6 to 16 antennas, and the VLA for 27 antennas. The top row shows images obtained with 6 antennas; row 2 has 10 antennas. Row 3 has the *uv* sampling which would be obtained with a 16 antenna combined array without cross correlations between 10.4 m and 6.1 m antennas. Row 4 is the combined array with all cross correlations. Row 5 is the 27 antenna

VLA scaled to the same resolution. The left column used a single frequency channel. The middle column shows the effect of the increased uv sampling which could be obtained with MFS synthesis using 20 frequency channels spanning an 8% bandwidth (8 Ghz at 100 GHz). Again we see the steady improvement in image fidelity as the uv sampling is increased. Column 3 shows the same MFS synthesis with the array size scaled $\times 2.5$. Here the large scale structure in the big E is resolved out, although we can still make out the letter because of the (astronomically unrealistic) sharp edges.

Figure 7 shows the eye chart imaged with the current 10-antenna BIMA array with 6.1 m antennas (left) and 15-antenna CARMA array with nine 6.1 m antennas and six 10.4 m antennas (right). The top row shows the mosaiced images with 19 pointings at 100 Ghz. The corners of the CARMA image are cut off by the smaller primary beam of the 10.4 m antennas. The middle row shows the deconvolved images using the MEM algorithm. The three primary beam patterns are modelled as Gaussians in the joint deconvolution. The RMS on the residual image (bottom row) is $3\times$ better with the CARMA array.

6.3. Effect of undersampled pointing

The Nyquist pointing interval is $\lambda/2D$ - roughly half the primary beam width. Undersampled pointing leads to aliasing of the uv data at spatial frequencies close to the antenna diameter. These are exactly the spatial frequencies which tie to those sampled directly by the shortest interferometer spacings. For simple source distributions, undersampled pointing allows us to observe a larger region in a fixed amount of time, but for complex source distributions we expect some degradation in the image fidelity. Figure 8 shows the effects of undersampling the pointing positions. The left column shows the mosaiced images with 19 pointings at 100 Ghz sampled at the Nyquist interval with 6.1 m antennas. The right column shows the same images and pointing sampling using the primary beam of the 10.4 m antennas. The middle row shows the deconvolved images. The RMS residual (bottom row) is 50% worse with the undersampled pointing positions.

6.4. Comparison of deconvolution algorithms

The CLEAN algorithm is well suited to deconvolving a field of point sources, but does a poor job with smooth extended source distributions. Conversely, maximum entropy algorithms are good at reconstructing smooth distributions, but do a poor job with compact bright features, as was seen on the moon like residual images of the Cas A models. The eye chart model falls between these two extremes; it has both extended structures and sharp features. We tried both the SDI clean algorithm (Steer, Dewdney & Ito 1984), and maximum entropy algorithms with the eye chart model. As expected, clean was better at reproducing the sharp features, and maximum entropy was better at reproducing the extended structures. We also tried separately deconvolving the individual pointings, and then combined the separately deconvolved subfields using a linear mosaic (a primary beam weighted average of all the pointings). For the eye chart model, which is composed of isolated structures, this worked quite well, and would be suitable for deconvolving an astronomical observation of a field of separated sources. Figure 9 shows a comparison of a linear mosaic and a MEM joint deconvolution (using the programs linmos and mosmem in MIRIAD). Both images were made with 19 pointings of an array consisting of sixteen 8 m antennas at 100 GHz. Left: Linear mosaic of the separately deconvolved pointings. Right: Joint Maximum Entropy deconvolution. The joint deconvolution has done a much better job recovering the large scale structure in the eye chart, and in reducing the sidelobe level. The linear mosaic was much much faster.

6.5. Heterogeneous versus homogeneous arrays

The CARMA array will have two or more different antenna diameters. The different primary beam patterns provide different weightings of the overall image (see Figure 4). One might expect that this would be an advantage in deconvolving a mosaiced image, as the same piece of sky is observed simultanously with different primary beams. There are two caveats. Firstly, pointing errors, or errors in the assumed primary beam patterns will introduce errors into the mosaiced image. Secondly, in comparison with a homogeneous array with the same number of antennas, each subfield of the heterogeneous array uses fewer antennas, and hence has poorer *uv* coverage. Too many primary beam types, resulting in sparse arrays, will almost certainly limit the image fidelity. Figure 10 shows a comparison of homogeneous and heterogeneous arrays with the same number of antennas and total collecting area. The left column shows images made with 19 pointings of a homogeneous array consisting of fifteen 8 m antennas at 100 GHz. The right column shows images made with 19 pointings of the heterogeneous, CARMA array, consisting of six 10.4 m and nine 6.1 m antennas. The overall RMS in the residual images (bottom row) is within 7% in both mosaics; the heterogeneous mosaic has better image fidelity of the eye chart letters, but worse RMS in the corners.

7. Conclusions

This empirical study of imaging with the merged array has explored a number of parameters. There are a large number of parameters to be explored. We imaged three representative models: eight point sources, Cas A, and an eye chart. In all three models, the image fidelity improved as the *uv* sampling was increased. More complex images require better *uv* sampling. MFS synthesis is an effective way to increase the *uv* sampling for continuum observations. Undersampling the pointing for mosaiced images degraded the image fidelity, although this might be suitable way to survey a large area of sky with a sparce distribution of sources. Although a joint deconvolution of mosaiced observations can recover *uv* spacings smaller than the minimum antenna spacing, the fidelity of the corresponding large scale structure was not so good. This has not been explored in any detail in this memo. A heterogeneous array allows shorter *uv* spacings to be sampled directly using a compact configuration of the smallest antennas. This reliably recovered more of the total flux density and the corresponding large scale structure. The heterogeneous CARMA array produced somewhat better image fidelity than a homogeneous array with the same number of antennas and collecting area.

REFERENCES

Cornwell, T.J., 1988, A&A 202, 316

Cornwell, T.J., 1989, Synthesis Imaging in Radio Astronomy. Ed. R.A. Perley, F.R. Schwab, & A.H.Bridle, ASP Conf. Ser. 6, 277

Ekers, R. D., & Rots, A.H. 1979, in IAU Col. 49, *Image Formation from Coherence Functions in Astronomy* , ed. van Schooneveld, C. (Dordrecht:Reidel), p.61

Mundy, L.G., " Configurations for the Joint Array", memo updated 1998 Mar 6.

Sault, R.J., Staveley-Smith, L & Brouw, W.N., 1996, A&A Supp., 120, 375

Steer, Dewdney & Ito 1984, A&A 137, 159

Wright, M.C.H., 1991, BIMA memo 45

Wright, M.C.H., 1997, Bima memo 59

This preprint was prepared with the AAS LaTeX macros v4.0.

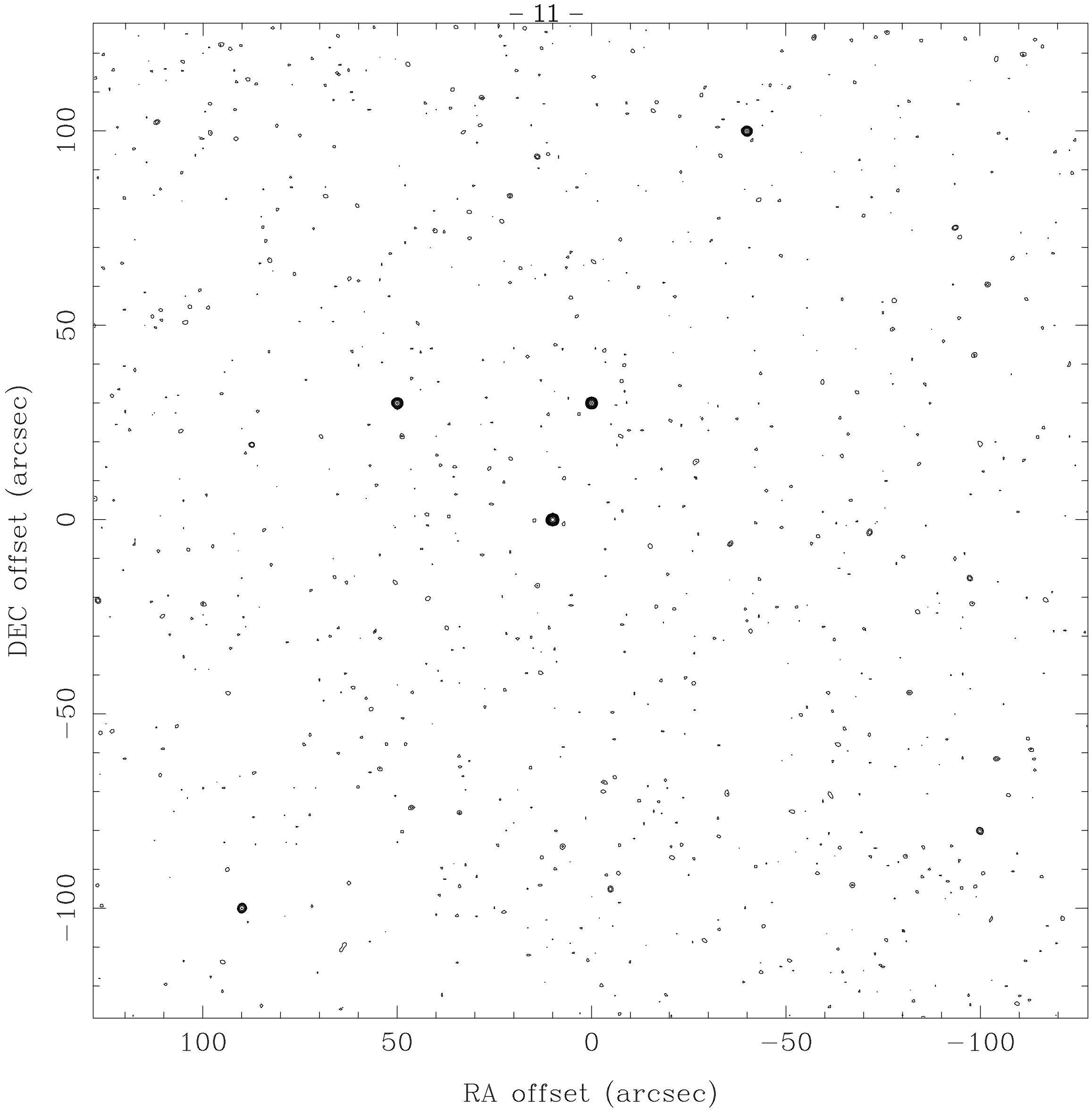

Fig. 1.— Eight point sources imaged with 1000 uv samples. Logarithmic contours starting at 1%. There are many spurious sources at the 1% level and a 20% error in the measured flux density of the 50 mJy source.

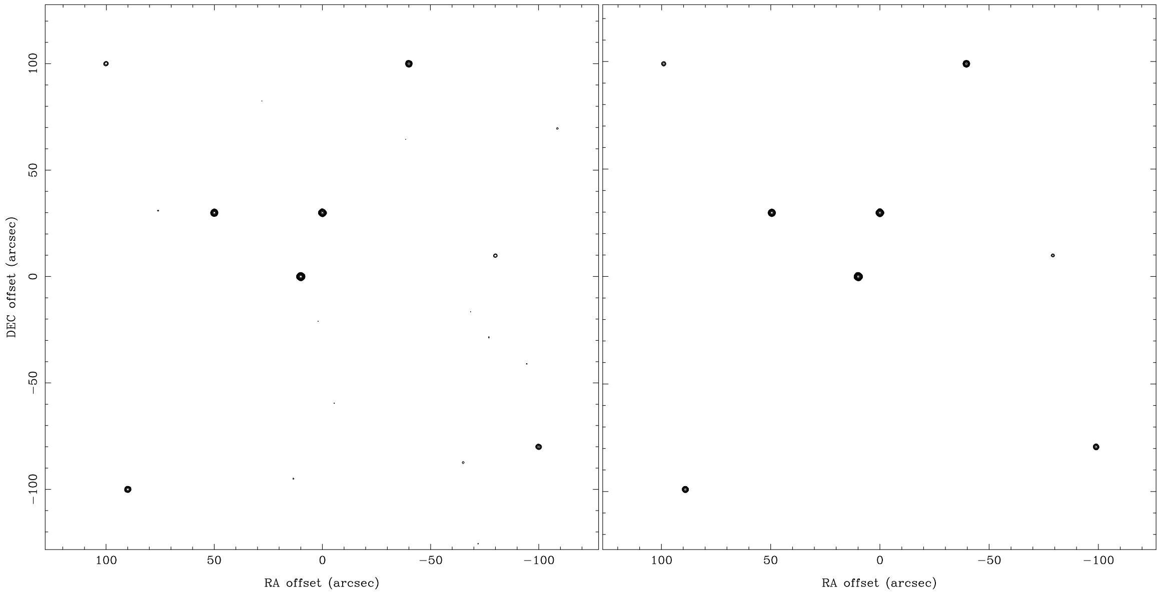

Fig. 2.— Eight point sources imaged with 2000 (left) and 4000 (right) uv samples. Logarithmic contours starting at 0.3%. With 2000 *uv* samples there are several spurious sources at the 0.3% level. With 4000 *uv* samples there are no spurious sources at the 0.3% level, although there is a 20% error in the measured flux density of the 10 mJy source.

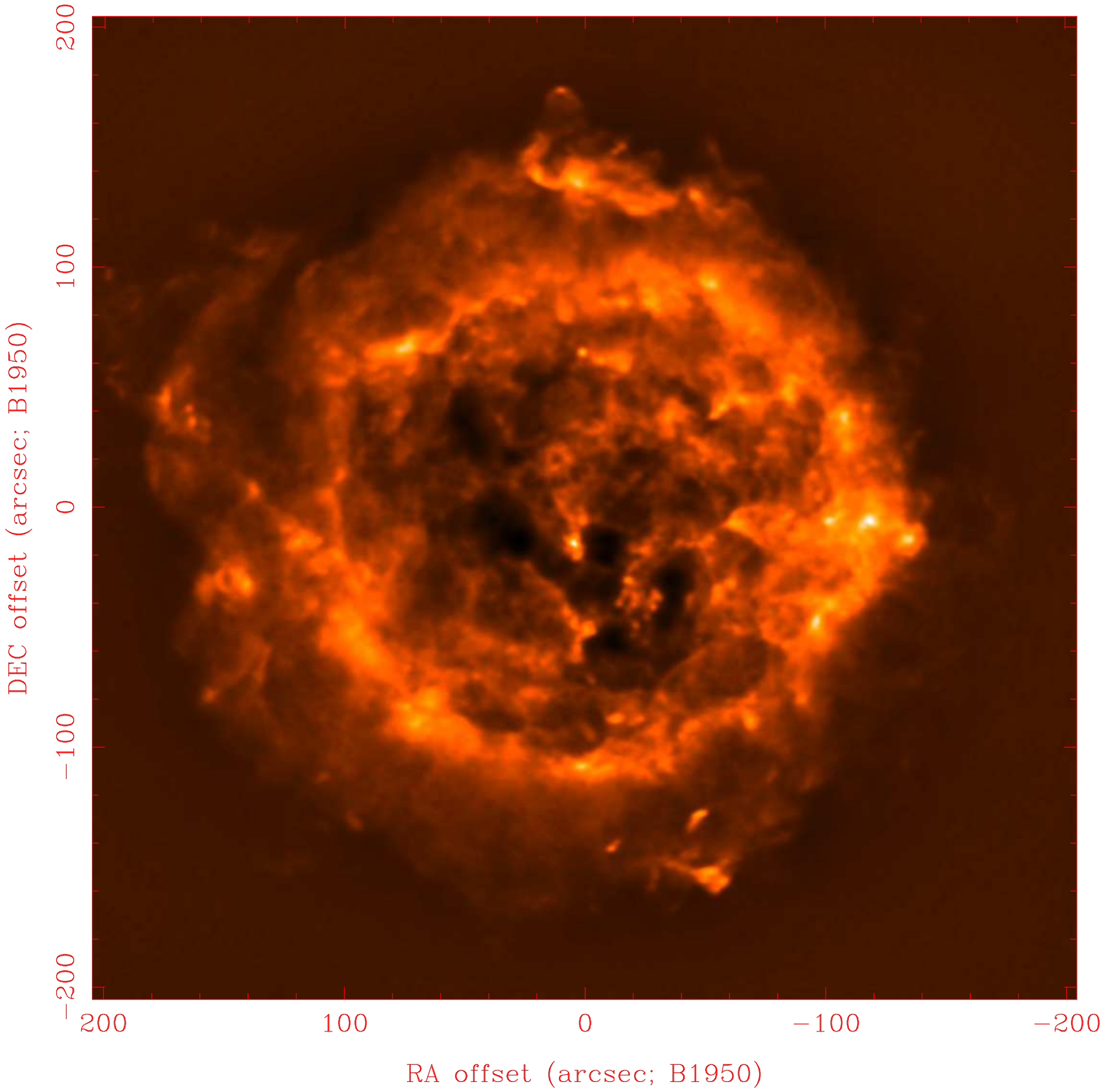

Fig. 3.— Model image of Cas A using observations at 4 configurations of CARMA and 2 frequency channels, 100 and 108 GHz. The resolution is $2.1'' \times 1.8''$

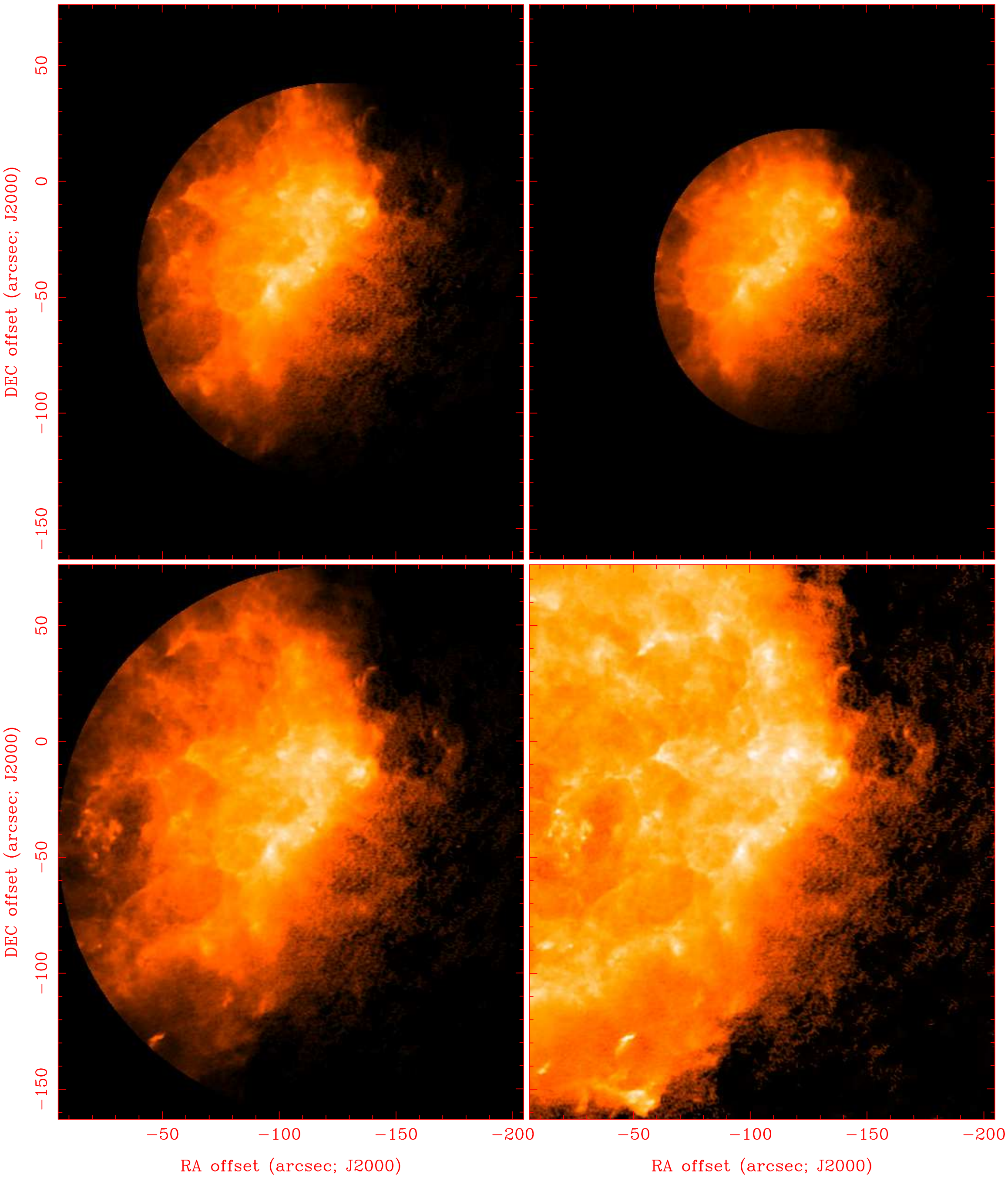

Fig. 4.— A single pointing on Cas A weighted by the primary beam pattern corresponding to 6.1 m (bottom left), 10.4 m (top right), and the cross correlation between 6.1 m and 10.4 m antennas (top left). Bottom right is the same field unweighted by any primary beam

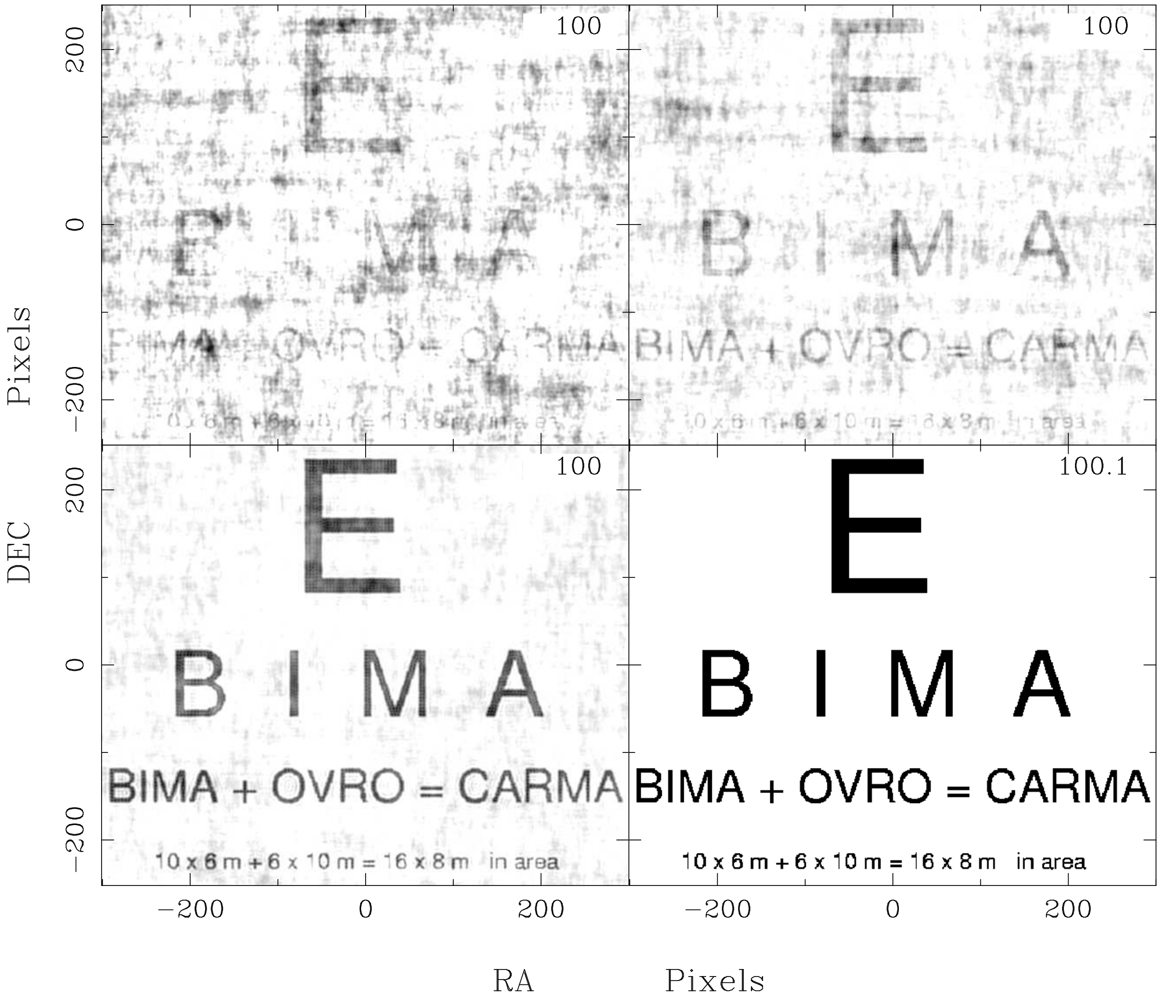

Fig. 5.— Effect of uv sampling on image fidelity with 5000 (top left), 10^4 (top right), 10^5 (bottom left) and 10^6 (bottom right) uv points

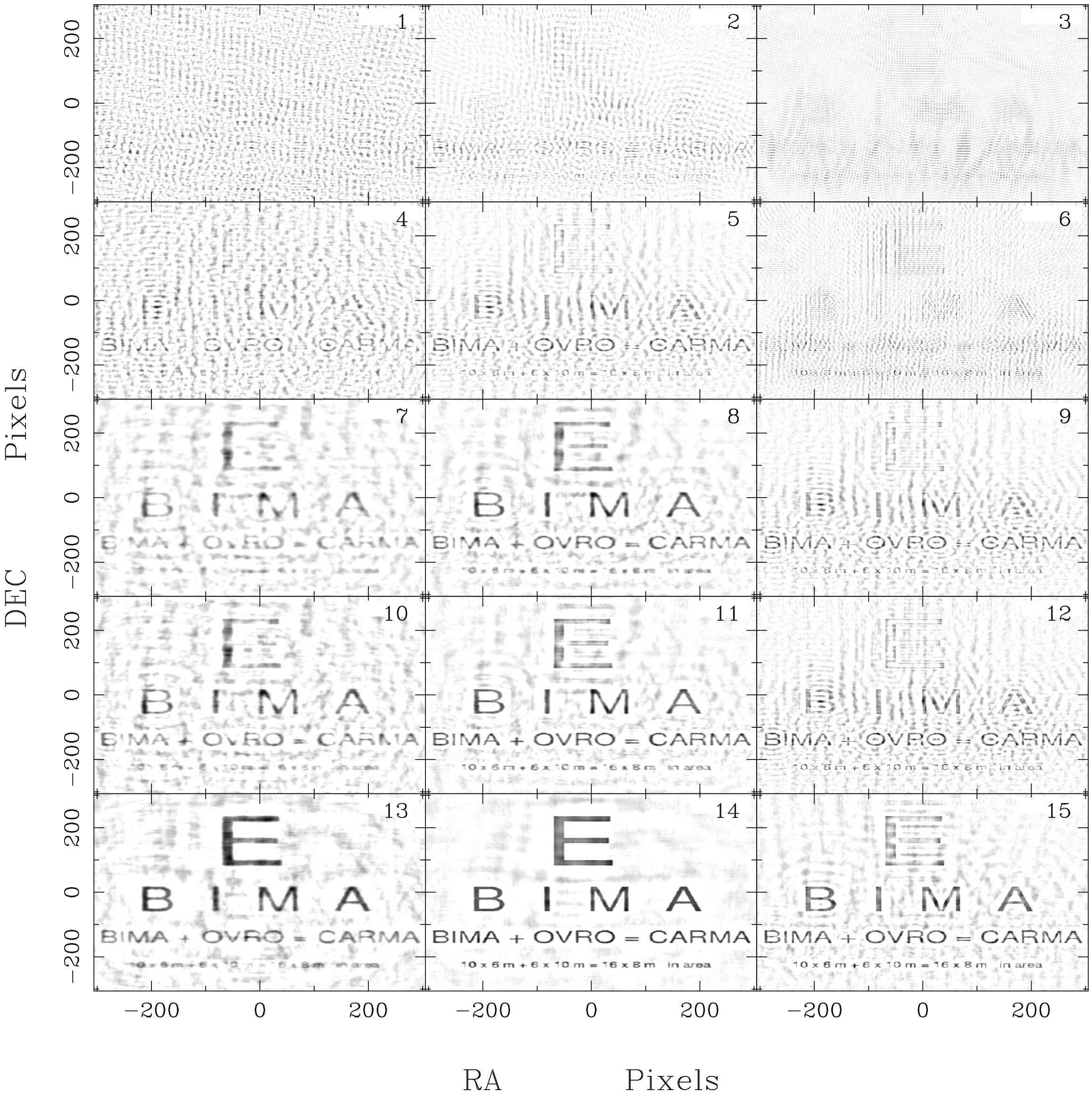

Fig. 6.— Eye chart imaged with different uv sampling: (row 1) six antennas, (row 2) ten antennas, (row 3) combined array without cross correlations between 10.4 m and 6.1 m antennas, (row 4) combined array with all cross correlations, (row 5) 27-antenna VLA scaled to the same resolution. (col 1) A single frequency, (col 2) MFS synthesis with 8% bandwidth, (col 3) MFS synthesis with array size scaled $\times 2.5$.

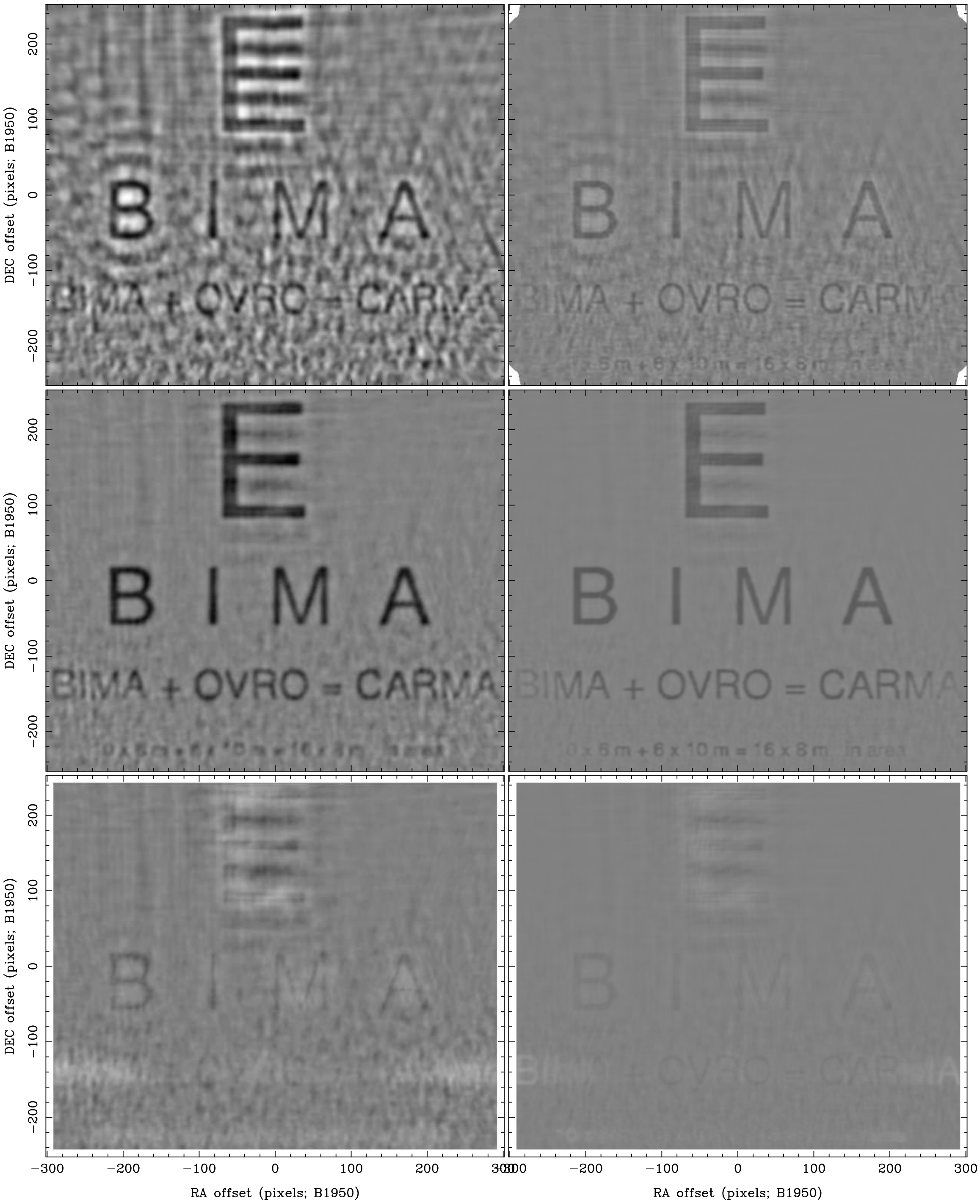

Fig. 7.— Eye chart imaged with current 10-antenna BIMA array (left) and 15-antenna CARMA array (right). Mosaic images imaged with 19 pointings at 100 Ghz (top row). Deconvolved images (middle row). The RMS residual (bottom row) is 3× better with the CARMA array.

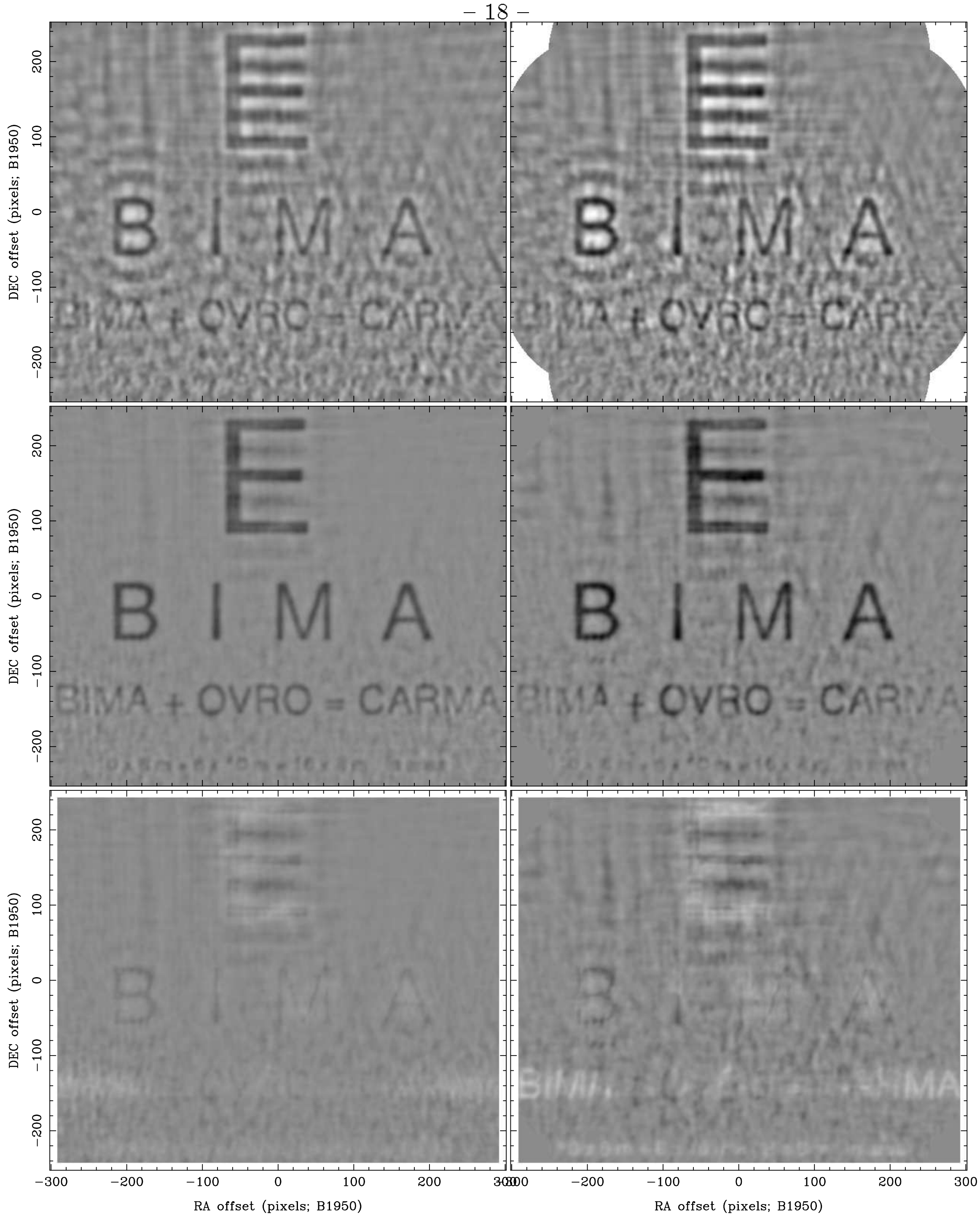

Fig. 8.— Effect of undersampling the pointing positions. The left column shows mosaic images with 19 pointings at 100 Ghz sampled at the Nyquist interval with 6.1 m antennas. The right column shows the same images and sample interval using the primary beam of the 10.4 m antennas. The middle row shows the deconvolved images. The RMS residual (bottom row) is 50% worse with the undersampled pointing positions.

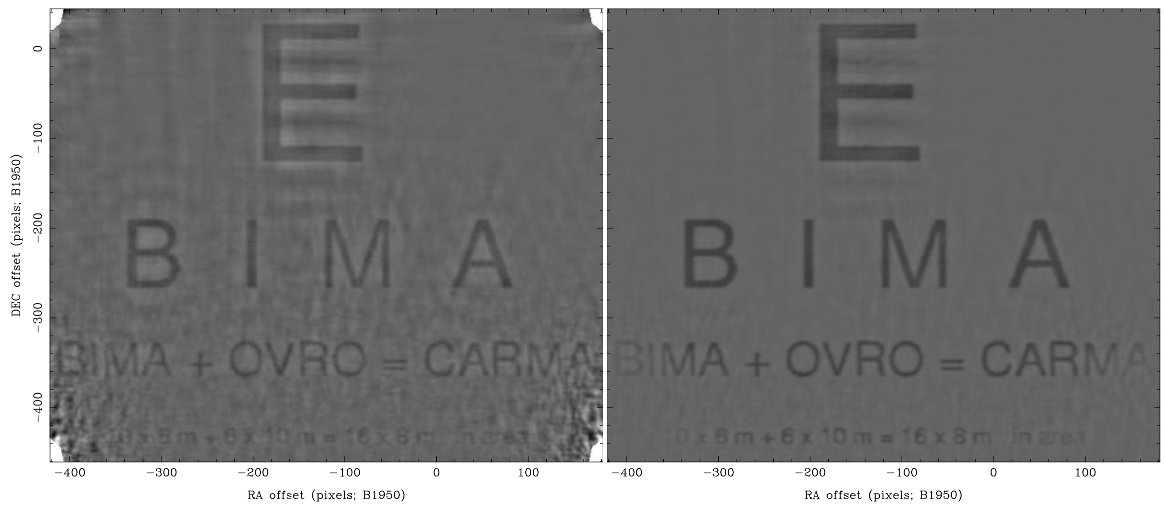

Fig. 9.— Comparison of linmos and mosmem. Both images were made with 19 pointings of an array consisting of sixteen 8 m antennas at 100 GHz. Left: Linear mosaic of the separately deconvolved pointings. Right: Joint Maximum Entropy deconvolution.

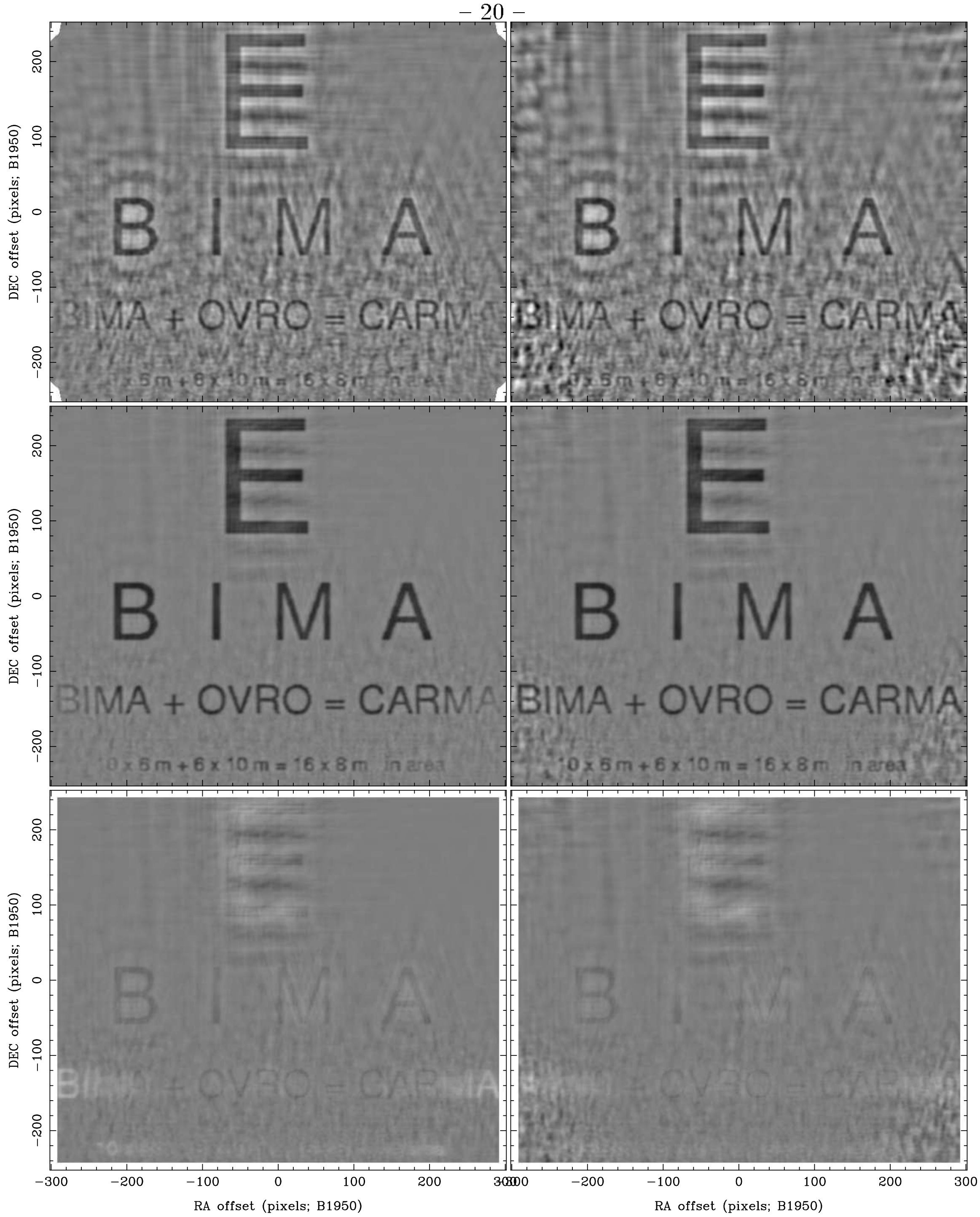

Fig. 10.— Comparison of homogeneous and heterogeneous arrays. Left column: Images made with 19 pointings of a homogeneous array consisting of fifteen 8 m antennas at 100 GHz. Right column: Images made with 19 pointings of the heterogeneous, CARMA array, consisting of six 10.4 m and nine 6.1 m antennas. The RMS residual (bottom row) is within 7% in both mosaics; the heterogeneous mosaic has better image fidelity of the eye chart letters, but worse RMS in the corners.